OPEN ACCESS
IOP Publishing
Classical and Quantum Gravity
Class. Quantum Grav. 37 (2020) 115004 (22pp)
https://doi.org/10.1088/1361-6382/ab857e

Local active isolation of the AEI-SAS for the AEI 10 m prototype facility

R Kirchhoff[1,2,5], **C M Mow-Lowry**[3], **G Bergmann**[1,2], **M M Hanke**[1,2], **P Koch**[1,2], **S M Köhlenbeck**[1,2], **S Leavey**[1,2], **J Lehmann**[1,2], **P Oppermann**[1,2], **J Wöhler**[1,2], **D S Wu**[1,2], **H Lück**[1,2] and **K A Strain**[1,4]

[1] Max Planck Institute for Gravitational Physics (Albert Einstein Institute), D-30167 Hanover, Germany
[2] Leibniz Universität Hannover, D-30167 Hanover, Germany
[3] School of Physics and Astronomy and Institute of Gravitational Wave Astronomy, University of Birmingham, Edgbaston, Birmingham B15 2TT, United Kingdom
[4] Scottish Universities Physics Alliance, School of Physics and Astronomy, University of Glasgow, Glasgow G12 8QQ, United Kingdom

E-mail: robin.kirchhoff@aei.mpg.de

Received 13 September 2019, revised 25 February 2020
Accepted for publication 1 April 2020
Published 4 May 2020

Abstract

High precision measurements in various applications rely on active seismic isolation to decouple the experiment from seismic motion; therefore, closed feed-back control techniques such as sensor blending and sensor correction are commonly implemented. This paper reviews the active isolation techniques of the Albert Einstein Institute seismic attenuation system (AEI-SAS). Two approaches to improve the well known techniques are presented. First, the influence of the sensor basis for the signal-to-noise ratio in the chosen coordinate system is calculated and second, a procedural optimization of blending filters to minimize the optical table velocity is performed. Active isolation techniques are adapted to the mechanical properties and the available sensors and actuators of the AEI-SAS. The performance of the final isolation is presented and limitations to the isolation are analyzed in comparison to a noise model. The optical table motion reaches approximately $8 \times 10^{-10}\,\mathrm{m}/\sqrt{\mathrm{Hz}}$ at 1 Hz, reducing the ground motion by a factor of approximately 100.

Keywords: active seismic isolation, AEI 10 m prototype, gravitational wave detection

---

[5] Author to whom any correspondence should be addressed.

1361-6382/20/115004+22$33.00

(Some figures may appear in colour only in the online journal)

1. Motivation

Gravitational wave (GW) detectors rely on the development and implementation of sophisticated technologies to suppress noise sources to achieve unprecedented sensitivity [1]. Prototyping facilities such as the Glasgow 10 m prototype [2], the MIT LIGO advanced system test interferometer [3] and the Caltech 40 m prototype interferometer [4] play a vital role in the development of these technologies by providing environments similar to a GW detector. The Albert Einstein Institute (AEI) 10 m prototype facility is currently under construction and will include a Fabry–Perot Michelson interferometer with ultra-low displacement noise using sophisticated seismic isolation systems. It will be housed in an L-shaped vacuum system with an arm length of approximately 10 m. The aim of the experiment is to reach and surpass the standard quantum limit (SQL) with macroscopic 100 g test masses. This requires classical noise to be reduced significantly below the SQL in a frequency band from 50–500 Hz [5]. The AEI 10 m prototype will be a valuable tool for investigating techniques to suppress quantum noise, which is already currently limiting the sensitivity of the Advanced LIGO detectors at frequencies above 50 Hz [1] and the Advanced Virgo detector above 100 Hz [6].

The isolation of seismic disturbances for the AEI 10 m prototype is essential to achieve its target sensitivity. This is realized using two different isolation systems. The AEI seismic attenuation system (AEI-SAS) [7, 8] provides seismically isolated optical tables with a focus on isolation in the frequency band from 0.1–10 Hz. Pendulum systems are placed on these optical tables and suspend the optics as shown in figure 1 to provide strong passive isolation in the measurement band [9]. The core optics of the interferometer, such as the test mass mirrors and the beam splitter, are suspended by three-stage suspensions to isolate them from seismic disturbances and actuation noise from actuators located above the final stage. The less critical auxiliary optics, such as beam steering mirrors, are suspended using one- or two-stage suspensions.

The passive isolation of the AEI-SAS is provided by two cascaded isolation stages, one for the horizontal and one for the vertical degrees of freedom, as shown in figure 1. The first stage provides the horizontal isolation using three inverted pendulum legs [10, 11]. This supports the vertical isolation stage which consists of three geometric anti-spring (GAS) filters [12]. Anti-spring techniques are used to tune the fundamental horizontal and vertical translational resonance frequencies down to 0.1 Hz and 0.3 Hz respectively. A Viton® stage is also implemented to damp internal resonances and support the optical table. Active isolation, which is the focus of this article, is provided by using coil-magnet actuators and a range of both inertial and relative motion sensors.

The AEI-SAS differs from other pre-isolation systems used in GW detectors in its mechanics, the set of installed sensors, and the methods implemented for active seismic isolation. The other systems can be divided into categories based on their similarity with the AEI-SAS:

- The TAMA-SAS [13], Virgo Superattenuator [14–16] and KAGRA-SAS [17] combine the pre-isolation system with the suspensions of the test masses without providing an optical table for auxiliary interferometer components.
- The HAM-ISI and BSC-ISI [18, 19] used for the Advanced LIGO detectors prioritize active isolation and are mechanically stiffer than the AEI-SAS.
- The MultiSAS of Advanced Virgo [20] uses similar techniques as the AEI-SAS but has the optical table suspended from above from a single wire. Its maximum payload mass is lower and it is less robust against payload dynamics.

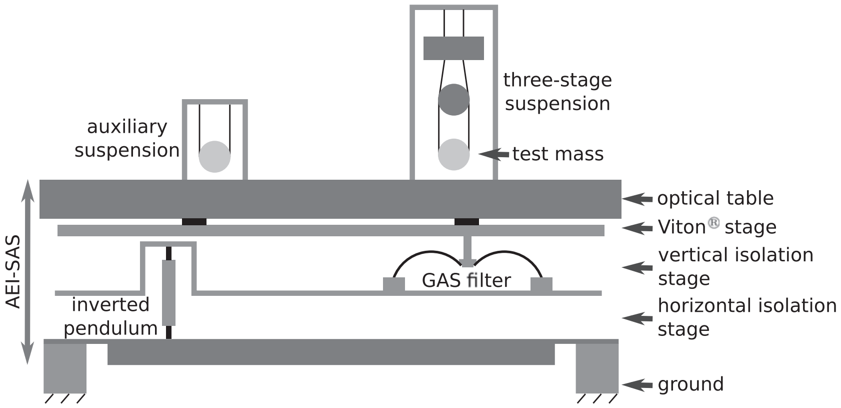

Figure 1. Diagram of a simplified AEI-SAS, a three-stage suspension, and a single-stage auxiliary suspension. Only a single inverted pendulum leg and GAS filter are shown.

- The EIB-SAS [21] of Advanced Virgo is similar to the AEI-SAS, but it does not operate in a vacuum system or support suspended optics. This relaxes the requirements on materials and on the isolation performance below 10 Hz.
- The HAM-SAS [22, 23], developed for Advanced LIGO, is the conceptual predecessor to the AEI-SAS and it has many similarities. It was, however, designed with 4 inverted pendulum legs and GAS filters. In the initial control strategy the HAM-SAS only employed relative motion sensors in feedback, the inertial isolation was derived from the passive response of the mirror suspension.

This article aims to provide detailed insight into the implementation of well known active control techniques like sensor blending and sensor correction [19] based on the noise of the utilized sensors and internal resonances of the mechanical system. This article also introduces novel approaches to improve well known active isolation techniques by considering the influence of the sensor alignment on the signal-to-noise ratio in different degrees of freedom (see section 4.3) and by minimizing the optical table velocity by optimizing the sensor blending (see section 4.4). The active control techniques discussed here are similar to those used for other pre-isolation systems and the presented techniques could be applied to those systems. The performance of the AEI-SAS is characterized through measurements of the optical table motion in section 5. The translational ground motion was attenuated by a factor of approximately 100 at 1 Hz reducing the optical table motion to $8 \times 10^{-10}\,\mathrm{m}/\sqrt{\mathrm{Hz}}$. Additionally, the performance of the vertical translational isolation is compared to a detailed noise model to analyze the limitations of the active control system.

2. Objectives of the active seismic isolation

The aim of the active control system of the AEI-SAS is to stabilize the SQL interferometer by reducing the differential arm velocity, rather than the inertial displacement of the individual optical tables. This approach led to the decision to minimize the velocity of the optical tables. Velocity increases proportionally with frequency compared to displacement. This results in an increased weighting of the frequency band containing the resonances of the optics suspensions (0.6–10 Hz), which have a stronger impact on the differential arm length than lower frequencies. Additionally, frequency up-conversion of scattered light can enter the interferometer and contaminate the interferometer readout in the measurement band [24]. This effect increases non-linearly with the velocity of the scatter source. Laser light scattered from components mounted on the AEI-SAS is expected to be a major noise source of the SQL interferometer and hence emphasis is placed on minimizing the velocity.

The reduction of the differential arm velocity of the SQL interferometer can be optimized by introducing common motion in the low frequency band. The three AEI-SASs respond similarly to ground motion below their lowest fundamental resonance frequency at 0.1 Hz. Consequently, the ground motion is similar for all three AEI-SAS at this frequency band as the corresponding coherence length of the seismic waves is significantly longer than the distance between the AEI-SAS. An active control scheme which forces the AEI-SAS to follow the ground motion at these frequencies could be optimal as the sensor noise for inertial sensors is relatively high at these frequencies. At frequencies above 0.1 Hz the AEI-SASs respond differently from one another to ground motion due to small mechanical differences in the tuning of the inverted pendulum legs and GAS filters, as well as manufacturing tolerances in the AEI-SAS components. This requires a minimization of the inertial motion of the individual optical tables at these frequencies.

3. Control scheme

The active isolation of the AEI-SAS is based on the combination of relative and inertial sensors into a 'super sensor' for each degree of freedom. A conceptual overview is provided in this section. The AEI-SAS control scheme is adapted from the Advanced LIGO control scheme for the mechanically soft HAM-SAS [23] and the HAM-ISI [19].

A block diagram of the overall local active control scheme of the AEI-SAS for a single Cartesian degree of freedom is given in figure 2. The ground motion, x_g, acts on the AEI-SAS labeled with 'plant'. The resulting plant motion, x_p, is measured by two different sensor types, the relative sensors, S_R, and the inertial sensors, S_I.

Relative sensors measure the differential position between the optical table of the AEI-SAS and the ground. They typically have lower noise at low frequencies than inertial sensors; hence, they are well suited for actively controlling the AEI-SAS below 0.1 Hz. Inertial signals can be approximated by sensor correction which is a feed-forward technique to subtract the ground motion from the signal of the relative sensors:

$$x_\mathrm{R} = x_\mathrm{p} - x_\mathrm{g} + n_\mathrm{R}, \tag{1}$$

$$x_\mathrm{G} = x_\mathrm{g} + n_\mathrm{G}, \tag{2}$$

$$x_\mathrm{R}^\mathrm{corr} = x_\mathrm{R} + x_\mathrm{G} = x_\mathrm{p} + n_\mathrm{R} + n_\mathrm{G}, \tag{3}$$

where $x_\mathrm{R}^\mathrm{corr}$ is the sensor corrected relative sensor signal, x_G is the signal of the ground motion sensor and n_R and n_G are the sensor noise contributions of the relative and the ground sensor respectively. x_G is filtered by a high-pass filter H_corr to attenuate its noise at frequencies below 0.04 Hz.

The inertial sensors used have a low noise at frequencies above 0.1 Hz, but cannot provide a DC position signal. They are combined with the relative sensors by frequency-dependent filtering and summation and form the super sensor S. The signal from the super sensor is processed by the controller, C, and sent to the actuators to correct the effect of ground motion. The following section discusses the implementation of this control scheme for the AEI-SAS.

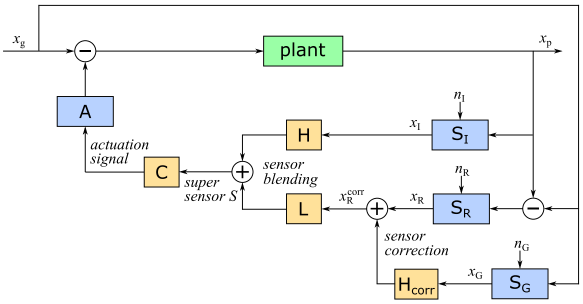

Figure 2. Block diagram of the local active control system for the AEI-SAS in a single degree of freedom. S_I labels the inertial sensors, S_R the relative sensors and S_G the ground motion sensor. x_I, x_R and x_G are the signals of the corresponding sensors. x_g is the ground motion, x_p the plant motion and x_R^{corr} the sensor corrected signal of the relative sensors. L and H are the low- and high-pass filters of the sensor blending, H_{corr} is the high pass filter for the sensor correction, C is the controller, A represents the actuators and n the sensor noise contributions.

4. Signal preparation

4.1. Sensors and actuators

The AEI-SAS is equipped with several sensors and actuators to realize the active control scheme. Linear variable differential transformers (LVDTs) [25] measure the relative position between the ground and the isolated stages. They are co-located with the inverted pendulum legs for the horizontal degrees of freedom and with the GAS filters for the vertical degrees of freedom. Each LVDT assembly contains a voice-coil actuator [26] capable of exerting force on the isolated stage; these are the actuators used in the active control. Three horizontal inertial sensors, the accelerometers [27], are positioned in an equilateral triangle in the spring box. Three vertical Sercel L-4C geophones are installed inside the optical table. In addition, there are three horizontal and four vertical motorized blade springs [7] which are used for coarse positioning of the optical table within 0.1 mm displacement of the desired operating point. They were not included into the control loops because of their high noise during use. A single Streckeisen STS-2 seismometer on the ground provides signals for feed-forward sensor correction (see section 4.5).

Figure 3 shows three different schematic representations of the AEI-SAS. Perspective (a) shows a top view of the simplified L-shaped vacuum system including the three AEI-SAS and their global coordinate system. The cross section view in (b) shows a simplified single AEI-SAS to show the vertical positioning of the various types of sensors and actuators. The top views of each stage of the AEI-SAS in (c) show the horizontal positioning of the sensors and actuators; however, the vertical geophones differed for each AEI-SAS due to the individual space constraints.

4.2. Active control noise

The main objective of the AEI-SAS is to stabilize the suspended optics of the SQL interferometer and can be optimized, as discussed in section 2, by forcing the tables to follow the ground motion at frequencies below 0.1 Hz. This is accomplished using the LVDTs which measure the relative displacement between the ground and the AEI-SAS. The residual relative motion between the AEI-SAS and the ground will be ultimately limited by electronic sensor noise of

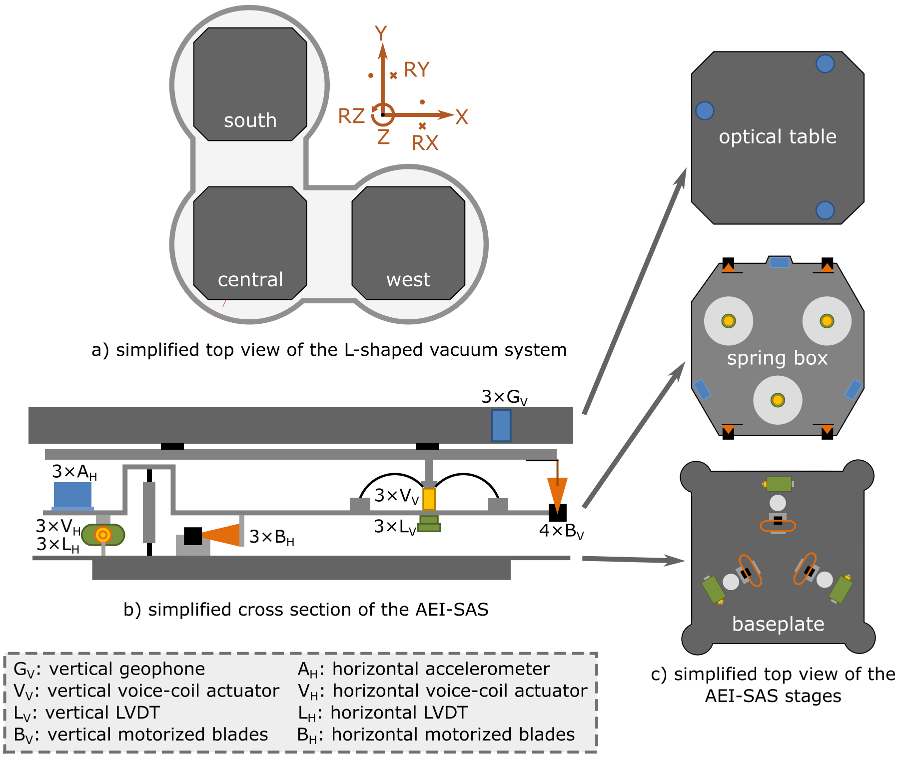
a) simplified top view of the L-shaped vacuum system

b) simplified cross section of the AEI-SAS

c) simplified top view of the AEI-SAS stages

Figure 3. Diagrams of the AEI-SAS illustrating: (a) their positions in the vacuum system; (b) a side view (Z–X plane) to show the vertical position of the sensors and actuators; (c) top views of each stage to show position of all sensors and actuators in the X–Y plane. The vertical geophone positions differ for each AEI-SAS and are shown here as an example.

the LVDT, provided the loop has sufficient gain. Above 0.1 Hz, inertial isolation of the table is preferred and hence the LVDT signal is considered 'unwanted' as it will be predominantly a measurement of the ground motion. We define the unwanted LVDT signal as the sensor noise at frequencies below 0.1 Hz, and as the sum of the residual measured ground motion after sensor correction and sensor noise above 0.1 Hz. It is shown in units of translation amplitude spectral densities (ASD) in figure 4. This could be considered as the effective noise of the LVDTs, despite not being strictly noise, as its use in a control loop degrades the AEI-SAS performance.

An overview of the predominant active control noise sources is shown in figure 5, which consists of the accelerometer noise, L-4C noise, and the unwanted LVDT signal. Appendix A provides details on all sensors implemented in the AEI-SASs and their noise. The noise of the accelerometers and L-4Cs were measured in huddle tests [28]. The voice-coil actuator noise below approximately 1 Hz is suppressed by the control loop, and at higher frequencies it is negligibly low compared to sensor noise. The actuator noise was therefore not included in figure 5.

4.3. Coordinate system transformation

The sensors used for the AEI-SAS measure translational motion along a single axis defined by their orientation. With linear combinations of multiple sensors it is possible to completely

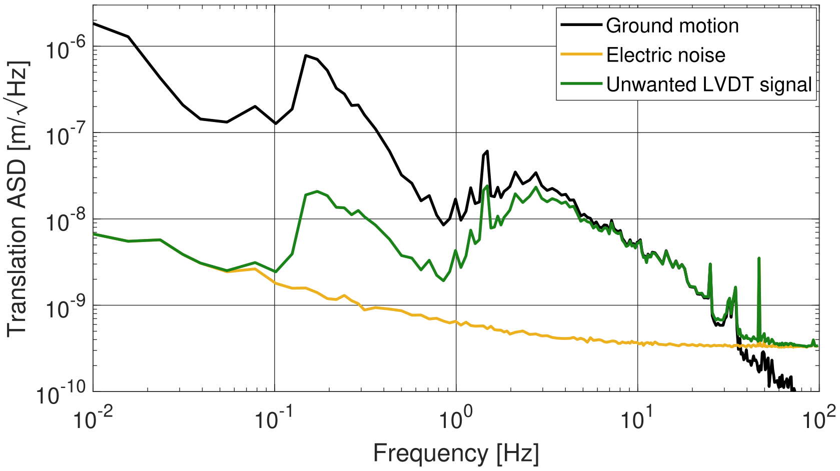

Figure 4. Unwanted signal of an LVDT. The ground motion is shown in black and has a typical amplitude for Hanover. The LVDT electrical noise floor is pictured in yellow and the unwanted LVDT signal is shown in green. The unwanted LVDT signal consists of the electrical noise below 0.1 Hz and of a combination of electrical noise and ground motion coupling to the LVDT above 0.1 Hz.

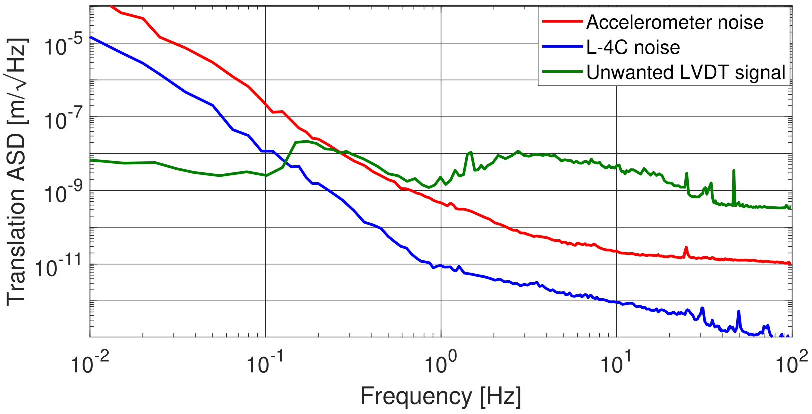

Figure 5. Sensor noise of the accelerometers and the L-4C geophones and unwanted LVDT signal, all calibrated to a displacement-equivalent spectral density. The unwanted LVDT signal is predominantly electrical noise below 0.1 Hz and a combination of electrical noise and ground motion coupling to the LVDT above 0.1 Hz.

describe the AEI-SAS motion. The global Cartesian coordinate system shown in figure 3 was chosen as the reference frame for the sensor orthogonalization, allowing for intuitive operation of the experiments at the AEI 10 m prototype. In the horizontal degrees of freedom, the coordinate transformation from the local sensor basis to the Cartesian basis is

$$\begin{pmatrix} X \\ Y \\ RZ \end{pmatrix} = \mathbb{M} \cdot \begin{pmatrix} H_1 \\ H_2 \\ H_3 \end{pmatrix}, \tag{4}$$

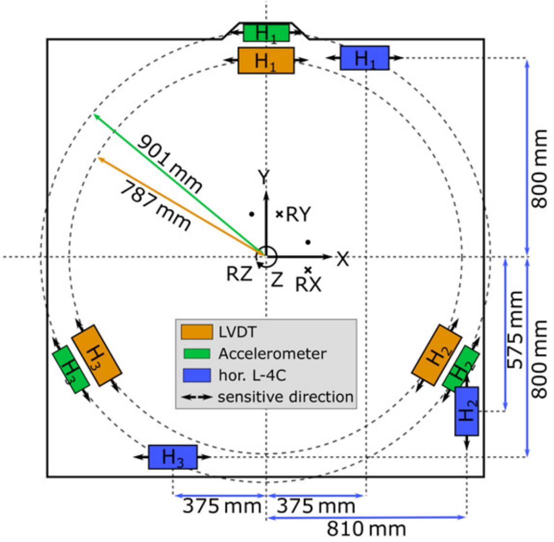

Figure 6. Alignment of horizontal sensors in the AEI-SAS. The figure shows the accelerometers, horizontal LVDTs and horizontal L-4Cs. Sensors of the same type lie on the same horizontal (X–Y) plane.

with

$$\mathbb{M} = \begin{pmatrix} H_{1,X} & H_{2,X} & H_{3,X} \\ H_{1,Y} & H_{2,Y} & H_{3,Y} \\ H_{1,RZ} & H_{2,RZ} & H_{3,RZ} \end{pmatrix}, \tag{5}$$

where X, Y and RZ are the components of the Cartesian coordinate system and, H_1, H_2 and H_3 is the measured motion of the individual sensors. The entries $H_{i,j}$ of the transformation matrix $\mathbb{M}$ describe how the output of sensor i contributes to degree of freedom j. The vertical degrees of freedom are calculated using the same procedure.

The contribution of signal from a sensor for a certain Cartesian degree of freedom depends on its alignment to this degree of freedom. In contrast, the noise contribution is independent of the alignment and fully couples to the sensor output. The effects of this can be understood intuitively with the following thought experiment using figure 6, which shows the positioning of the horizontal sensors for the AEI-SAS. Consider motion of the AEI-SAS in the Y direction and that only the horizontal L-4C geophones, which are a planned future upgrade, are to be used to measure this. H_2 is the only sensor which is aligned along the Y-axis and hence contributes to the Y signal with $H_{2,Y} \neq 0$. H_1 and H_3 also contribute to the Y signal with $H_{1,Y}, H_{3,Y} \neq 0$ as they are required to subtract a possible RZ motion which would also be measured by H_2. The noise from these sensors however is uncorrelated and does not subtract. Therefore, the noise from all three sensors contribute to the Y measurement, despite only H_2 contributing the desired signal.

The signal-to-noise ratio (SNR) for the degree of freedom $j = \{X, Y, RZ\}$ can be calculated as:

$$\mathrm{SNR}_j = \frac{X_j}{n_{\mathrm{sensor}}} \cdot T_j \tag{6}$$

Table 1. T for the accelerometers, the horizontal LVDTs and the horizontal L-4Cs. The calculations refer to figure 6.

Sensor type	T_X	T_Y	T_{RZ}
Accelerometers	1.2247	1.2247	1.5606
LVDTs	1.2247	1.2247	1.3631
L-4Cs	1.4142	0.8117	1.1314

where X_j represents the signal in j, n_{sensor} is the noise of a single sensor under investigation and T_j is the multiplication factor depending on the alignment of the sensors to j. T_j is calculated as

$$T_X = \sum_{i=1}^{3} \frac{H_{i,X} \cdot (\hat{x} \cdot \hat{h}_i)}{\sqrt{(H_{1,X})^2 + (H_{2,X})^2 + (H_{3,X})^2}} \tag{7}$$

$$T_Y = \sum_{i=1}^{3} \frac{H_{i,Y} \cdot (\hat{y} \cdot \hat{h}_i)}{\sqrt{(H_{1,Y})^2 + (H_{2,Y})^2 + (H_{3,Y})^2}} \tag{8}$$

$$T_{RZ} = \sum_{i=1}^{3} \frac{H_{i,RZ} \cdot ((\vec{r}_i \times \hat{z}) \cdot \hat{h}_i)}{\sqrt{(H_{1,RZ})^2 + (H_{2,RZ})^2 + (H_{3,RZ})^2}} \tag{9}$$

where $i = \{1, 2, 3\}$ labels the sensors, $H_{i,j}$ describes the entries of $\mathbb{M}$, $\hat{x}$, $\hat{y}$ and $\hat{z}$ define unit vectors in X, Y and Z. $\hat{h}_i$ is the unit vector pointing into the sensitive direction of sensor i and $\vec{r}$ is the position vector of the sensor i in the X–Y plane from the Z-axis. The quantities $\hat{x} \cdot \hat{h}_i$, $\hat{y} \cdot \hat{h}_i$ and $(\vec{r}_i \times \hat{z}) \cdot \hat{h}_i$ are projections of the sensitive direction of the sensors onto the degree of freedom under investigation.

Table 1 provides the values of T for the different sets of horizontal sensors corresponding to the positions in figure 6. The accelerometers and LVDTs are positioned on circles with different radii from the Z-axis but with the same orientations. This results in an equal T_X and T_Y, but a larger T_{RZ} for the accelerometers due to the larger $|\vec{r}|$. The position of the L-4Cs results in a larger T_X than the other sensor sets, but at the cost of smaller T_Y and T_{RZ}.

These calculations show that the geometry of the sensors can be adapted to the needs of the active control system in order to optimize the SNR. In GW interferometers, for example, the longitudinal motion of the optics is more important than the lateral motion because it couples stronger to the interferometer readout. Choosing a beneficial sensor basis for the longitudinal motion can therefore increase the interferometer sensitivity. In cases where all degrees of freedom are equally important, such as the central AEI-SAS, the equilateral triangle is the best choice for three sensors.

The sensor alignment for the AEI-SASs is fixed and can not be optimized due to space constrains on the optical tables. For the AEI-SAS, the calculation of T_j is solely utilized for a precise estimation of limitations for the active isolation performance demonstrated in section 5. The sensor alignment should be taken into account when designing new pre-isolation systems.

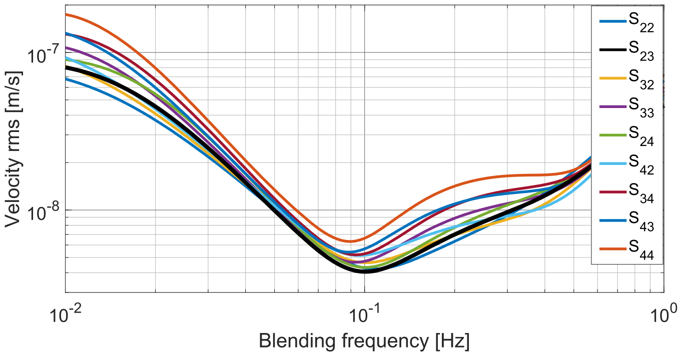

Figure 7. Super sensor velocity rms in Z for combinations of low- and high-pass filters of order 2, 3 and 4. The optimal blending parameters for vertical LVDTs and L-4C geophones are a 2nd order low-pass and a 3rd order high-pass filter (black) with a blending frequency of 0.1 Hz.

4.4. Sensor blending

LVDTs and inertial sensors are blended together to form the super sensor, S [19]. The super sensor features low noise of the inertial sensors at high frequencies while replacing the high noise of the same by the lower effective noise of the LVDTs at low frequencies as demonstrated in figure 5. The method for calculating blending filters is provided in appendix B.

Optimal sensor blending for the control system of the AEI-SAS requires the optimization of three parameters: the blending frequency, the low-pass order and the high-pass order. The calculation of these parameters is explained here for the specific case of blending sensor-corrected LVDTs and L-4Cs in the Z degree of freedom, but it is also applicable to the other cases of sensor blending in the AEI-SAS as well as in other seismic pre-isolation systems.

Multiple sets of blending filters $L_{l,h}$ and $H_{l,h}$ for blending frequencies f_{b} between 0.01–1 Hz and filter orders of 2, 3 and 4 were calculated. The goal of the blending filters is to strongly attenuate the signal from a particular sensor at the frequencies where noise or unwanted signal is dominant. A maximum order of 4 was chosen as the magnitude of the ripple around the blending frequency increases for higher order filters (see figure B1). This ripple amplifies the uncorrelated noise of the two blended signals. The subscripts l and h refer to the order of the low-pass and high-pass filters, respectively. The amplitude spectral density of the unwanted LVDT signal (n_{LVDT}) and the L-4C noise (n_{L4C}) were converted to velocity and multiplied with the low- and high-pass filters. The two contributions can be combined into the super sensor, and its rms velocity $|S_{\mathrm{lh}}(f_{\mathrm{b}})|_{\mathrm{rms}}$ can be calculated as:

$$|S_{\mathrm{lh}}(f_{\mathrm{b}})|_{\mathrm{rms}} = \int_{f=f_{\min}}^{f=f_{\max}} 2\pi f \,[n_{\mathrm{LVDT}}^{2}(f) {L_{\mathrm{lh}}}^{2}(f, f_{\mathrm{b}}) + n_{\mathrm{L4C}}^{2}(f) H_{\mathrm{lh}}^{2}(f, f_{\mathrm{b}})]^{1/2}\, \mathrm{d}f. \tag{10}$$

The symbols $f_{\min}$ and $f_{\max}$ define the frequency band of interest and correspond to 0 Hz and 100 Hz for the calculations in this paper. The velocity rms was calculated and used as the cost function for optimization. Figure 7 shows the resulting rms over the different blending frequencies for several blending filter combinations. The optimal combination of blending frequency and filter order with the minimum velocity rms was given by a 2nd order low- and 3rd order

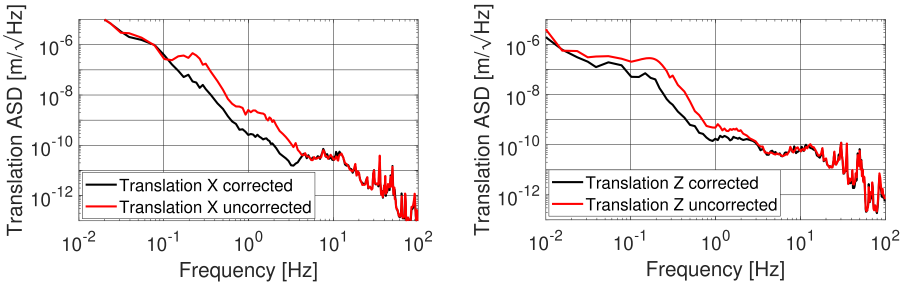

Figure 8. Measurements of the inertial west optical table motion with and without sensor correction in X on the left hand side and Z on the right hand side. Below 0.1 Hz in X and 0.04 Hz in Z, the sensor noise was limiting the measurement. Effects from the sensor correction are not visible below these frequencies.

high-pass filter with a blending frequency of 0.1 Hz. The resulting velocity rms disturbance for the LVDT/L-4C vertical super sensor was 4.06×10^{-9} m s^{-1}.

4.5. Sensor correction

The unwanted LVDT contribution to the super sensors above the blending frequency will still be significantly larger than the noise of the inertial sensors, despite the low-pass filtering. The unwanted LVDT signal is dominated by ground motion relative to the isolated platform above the lowest fundamental resonance frequency of 0.1 Hz. The ground motion can be independently measured using a seismometer placed on the ground and removed from the LVDT measurement to approximate an inertial sensor [19] (see equation (3)). This technique is called sensor correction and is applied to all AEI-SAS LVDTs using the measured ground motion from a single common STS-2. The effectiveness of sensor correction depends on the coherence between the STS-2 and the LVDTs and their relative calibration. At frequencies below approximately 0.04 Hz this is limited by the STS-2 noise rising with $1/f^3$ in the vertical and $1/f^5$ in the horizontal degrees of freedom due to the presence of tilt-to-horizontal coupling [29]. The sensor correction signal is therefore filtered by a high-pass filter in order to attenuate this noise. At frequencies above approximately 3 Hz the distance between the STS-2 and the LVDTs results in a loss of coherence between the sensors. The sensor correction is therefore effective for the frequency range from 0.04–3 Hz.

Figure 8 shows the results of the sensor correction in X and Z for the inertial displacement by measuring the inertial table motion with out-of-loop geophones. The improvement was up to a factor 10 and was achieved between 0.1–4 Hz in X and between 0.04–1 Hz in Z. At frequencies below 0.1 Hz in X and 0.04 Hz in Z the measurement was limited by the noise of the witness geophones and hence does not correspond to real table motion.

4.6. Controller

The signal conditioning discussed in sections 4.3–4.5 normalizes and blends the sensor signals to generate an error signal for each degree of freedom with the lowest possible noise given the available sensors. The controller processes the error signal to generate a feedback signal for the actuators which minimizes the optical table motion.

At frequencies above approximately 5 Hz, internal structural resonances of the AEI-SAS couple to the optical table motion. These resonances enhance the open loop gain at those frequencies while simultaneously adding a phase shift. If the gain is enhanced above unity

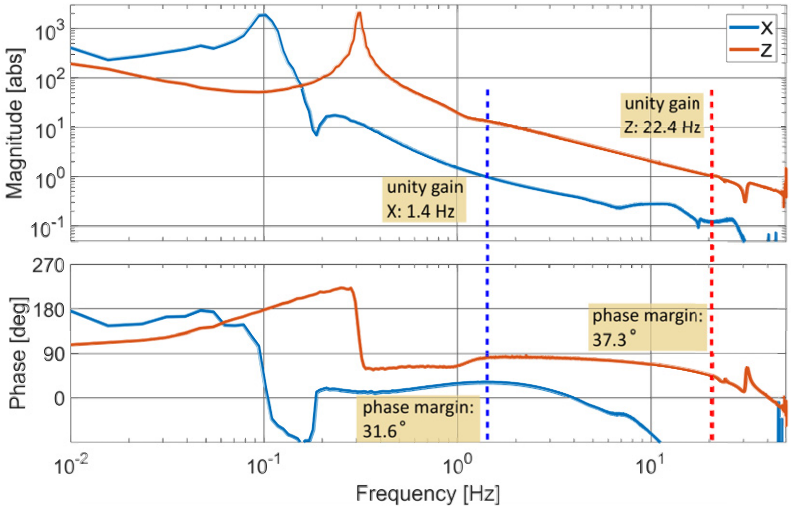

Figure 9. Bode plot for the open loop gain of the west AEI-SAS in X and Z. The unity gain frequencies of both degrees of freedom are marked and the phase margin is noted. The peaks at roughly 0.1 Hz and 0.3 Hz result from the mechanical resonances of the AEI-SAS. Above 50 Hz the coherence between the excitation and the measurement is low and the measurements lose their significance.

gain, this can result in instability. The controller gain was therefore rolled off with increasing frequency to prevent these internal resonances from crossing unity gain.

As the last to be built, the west AEI-SAS received various improvements compared to the other two AEI-SAS [8]. The internal structure was stiffened to increase the frequencies of the internal resonances, and additional damping was implemented to reduce the Q-factor of these resonances. These improvements enabled higher control bandwidths to be used and thus a better suppression of ground motion on the west AEI-SAS compared to the other two AEI-SAS.

Figure 9 shows measurements of the open loop gain of the west AEI-SAS for X and Z. The measurements include mechanical transfer functions and internal resonances. To allow for stability in the presence of changing seismic motion and temperature, the unity gain frequency was set to 1.4 Hz in X and to 22.4 Hz in Z to give a conservative phase margin in the loops. The discrepancy between the unity gain frequencies in X and Z results mainly from the horizontal accelerometers being located inside the mechanically soft spring box, while the vertical geophones are located on the comparably stiff optical table. Internal resonances inside the spring box couple directly to the accelerometers, whereas they are filtered by the GAS filters and the Viton® stage for the geophones. In a future upgrade, horizontal L-4C geophones placed on the optical table will replace the accelerometers. This will enable a higher control bandwidth in the horizontal degrees of freedom.

5. Characterization of the control scheme

The performance of the active isolation of the west AEI-SAS was characterized by measuring the inertial motion of the optical table and comparing it against the ground motion. The

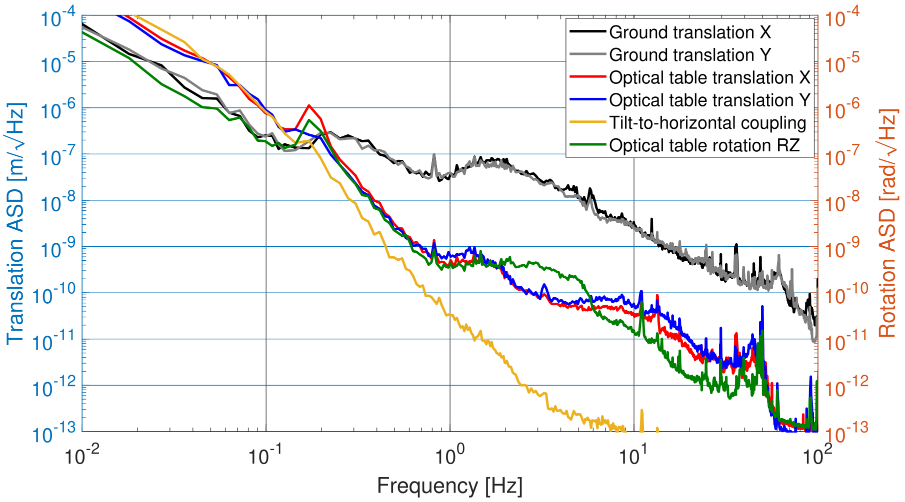

Figure 10. Horizontal inertial motion of the actively controlled optical table and horizontal ground motion. The tilt-to-horizontal coupling is calibrated in units of $\mathrm{m}/\sqrt{\mathrm{Hz}}$. The X and Y measurements are dominated by tilt-to-horizontal coupling below 0.13 Hz. For the in-loop geophones the signal is attenuated by the blending filter below the blending frequency but still limits the low frequency performance. The peak at 0.18 Hz is believed to be caused by the active control signal of the accelerometers and will be investigated when the accelerometers are replaced with horizontal L-4C geophones.

table motion was measured by using horizontal and vertical L-4C geophones, while the ground motion was measured using the STS-2 located 11 m away from the measured AEI-SAS. The horizontal L-4Cs were out-of-loop witness sensors, while the vertical geophones were the in-loop sensors. We are confident that the vertical in-loop measurements correspond to the residual table motion as the signals were significantly higher than the sensor noise [28]. The measurements were performed on a day with typical seismic activity.

The inertial optical table motion is shown in figures 10 and 11 for the horizontal and vertical degrees of freedom respectively. The tilt-to-horizontal coupling of the witness geophones [29] limited the measurements in X and Y below 0.13 Hz. The tilt-to-horizontal coupling is calculated using optical lever measurements of the optical table tilt motion [30]. The blending filters attenuate this coupling for the in-loop geophones below the blending frequency but it still limits the active isolation performance. The peaks at 0.18 Hz were believed to result from the active isolation signal of the accelerometers and will be investigated when the accelerometers are replaced by horizontal L-4C geophones located on the optical table in a future upgrade.

The measurements for all three vertical degrees of freedom below 0.03 Hz were dominated by the L-4C noise. This noise is not expected to imprint additional motion onto the optical table motion, despite being in-loop sensors, due to the sensor blending. The 11 Hz peak was likely due to a resonance of mechanical parts or cables on the optical table which bypass the isolation of the AEI-SAS between table and ground.

The measurement for the Z degree of freedom was additionally compared against a measurement of the uncontrolled AEI-SAS in figure 12. This shows the additional ground motion suppression achieved by the active system between approximately 0.1 Hz and 10 Hz compared to the purely passive isolation. In particular, it shows strong suppression of the enhanced table motion due to the GAS filter resonance at 0.3 Hz.

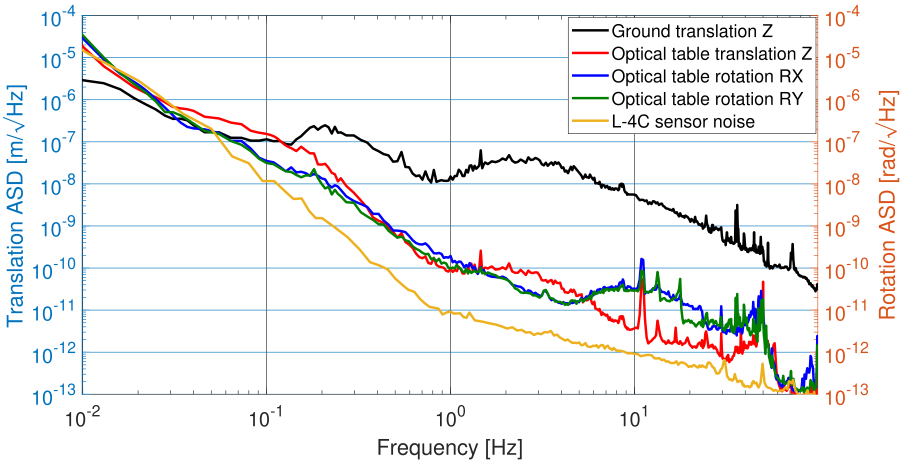

Figure 11. Vertical inertial motion of the actively controlled optical table and vertical ground motion. The L-4C sensor noise is calibrated in units of $\mathrm{m}/\sqrt{\mathrm{Hz}}$. Below 0.3 Hz the sensor signals are sensor noise limited and hence do not show real table motion. This does not influence the isolation as the L-4C signal is attenuated by the blending filters. At 11 Hz the measurements show a resonance which is subject of future investigations.

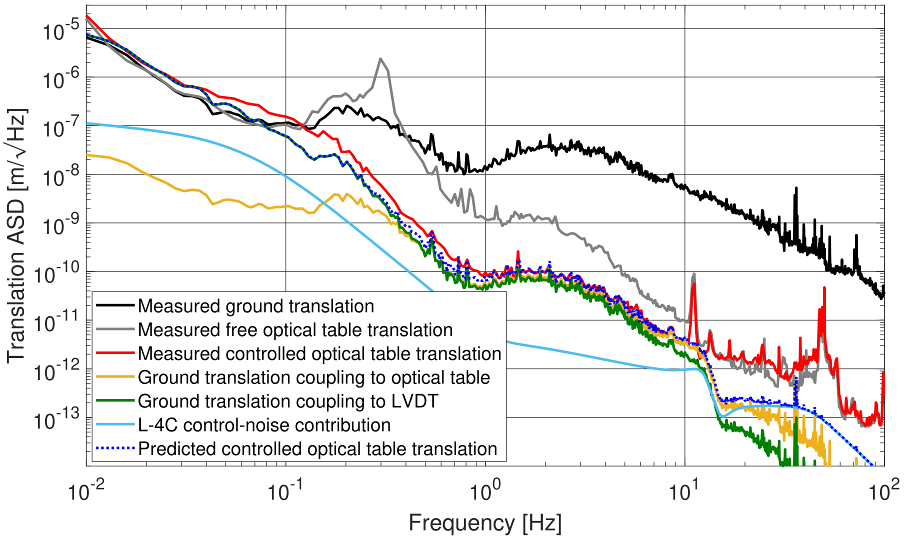

Figure 12. Measurement of the inertial optical table motion and noise contributions in Z. The red curve shows a measurement of the inertial motion using all the active control techniques explained in this article. The AEI-SAS performance in Z was also simulated and the relevant noise sources are included. Below approximately 0.35 Hz ground motion coupling to the LVDTs limits the isolation. Above 0.35 Hz it is the unsuppressed ground motion and the ground motion coupling to the LVDTs. Above 10 Hz the simulation does not reproduce the measured data.

The measurement was additionally compared against a model of the AEI-SAS to understand the limiting factors for the active system. The model included the sensors, controllers, actuators and the mechanical response of the AEI-SAS (the plant). The expected performance was simulated using SimulinkNb [31] by injecting measurements of the ground motion and sensor noise into the model. The blue trace in figure 12 shows the sum of all modeled contributions and thus represents the predicted inertial optical table motion. The model shows that the performance was limited by ground motion coupling to the LVDT output below 0.35 Hz. The optical table follows the ground below 0.1 Hz which was desired as motion at low frequencies is expected to be common motion for all the AEI-SAS, as discussed in section 2. Above 0.35 Hz, the performance was limited by a combination of residual ground motion due to insufficient loop gain, which was set for stability robustness; and by ground motion coupling to the LVDTs, which was already optimized by the choice of blending filters and by sensor correction. The discrepancy between the model and measurement above 10 Hz is believed to be due to the internal resonances of the AEI-SAS, which were not included in the model.

6. Conclusion

Two approaches to optimize the local active isolation of the AEI-SAS using standard control techniques were presented. First, the influence of the local sensor basis due to the positioning and orientation of the individual sensors on the signal-to-noise ratio in the Cartesian degrees of freedom was discussed. Second, the calculation of the optimal blending filters based on the minimization of velocity noise was demonstrated.

The overall performance of the west AEI-SAS active isolation was measured. The optical table motion was attenuated by a factor of approximately 100 to reduce the optical table motion to a maximum displacement of $8 \times 10^{-10}\,\mathrm{m}/\sqrt{\mathrm{Hz}}$ at 1 Hz in every translational degree of freedom. This provides effective pre-isolation for the mirror suspensions and auxiliary optics. In the vertical degree of freedom, Z, the performance was further analyzed by comparing it against a noise model. The measurement and prediction had good agreement at frequencies below 10 Hz. This showed that the residual motion is limited by both the loop gain and the coupling of ground motion to the LVDTs, both of which were already optimized for stability and performance.

In the current configuration the AEI-SASs fulfill their goal in providing a quiet environment for the interferometer suspensions, the auxiliary interferometer optics, and the other sub-systems. More detailed isolation requirements were never set. Future improvements like the global control scheme with optical levers and suspension platform interferometers [30] will provide further advantages such as reducing the required forces applied by the suspension actuators and lowering scattering noise.

Acknowledgments

The authors gratefully thank the International Max Planck Research School (IMPRS) on Gravitational Wave Astronomy, QUEST, the Center for Quantum Engineering and Space-Time Research and Quantum Frontiers, the Deutsche Forschungsgemeinschaft (DFG, German Research Foundation) under Germany's Excellence Strategy EXC-2123 QuantumFrontiers 390837967 for their support.

Appendix A. Active control noise sources

This appendix discusses the various noise sources to the active isolation of the AEI-SAS.

The various sensors utilized in the AEI-SAS have different operating principles but share similar noise sources. The readout electronics for the sensors use various amplifiers which contribute voltage and current noise, $n_{\mathrm{v}}(\omega)$ and $n_{\mathrm{c}}(\omega)$ respectively. Wire coils are utilized to sense the motion and contribute non-negligible Johnson noise, $n_{\mathrm{J}}(\omega)$. The inertial sensors use suspended masses as harmonic oscillators which additionally adds a thermal suspension noise contribution, $n_{\mathrm{s}}(\omega)$. A detailed noise model for geophones is presented in [32] and a similar approach can be used to model the noise for every sensor used in the AEI-SAS. These noise contributions can be expressed in units of equivalent displacement noise, m/$\sqrt{\mathrm{Hz}}$, by multiplying the noise with the appropriate response functions for the sensors:

$$\begin{aligned} n_{\mathrm{s}}(\omega) &= \left(\frac{4k_{\mathrm{b}}T\omega_0}{mQ}\right)^{1/2}\cdot\frac{1}{\omega^2},\\ n_{\mathrm{J}}(\omega) &= \frac{(4k_{\mathrm{b}}T\Re(Z))^{1/2}}{\tilde{X}(\omega)},\\ n_{\mathrm{v}}(\omega) &= \frac{N_{\mathrm{V}}(\omega)}{\tilde{X}(\omega)},\\ n_{\mathrm{c}}(\omega) &= \frac{N_{\mathrm{A}}(\omega)\Re(Z)}{\tilde{X}(\omega)}. \end{aligned} \tag{A.1}$$

where ω is the angular frequency. Each noise contribution is uncorrelated and hence the total noise of a sensor or actuator is given by the incoherent sum of the various contributions.

T	Temperature (K)
$\omega_0 = 2\pi f_0$	Angular resonance frequency of the mechanical spring (Hz)
m	Suspended mass (kg)
Q	Quality factor
$\tilde{X}(\omega)$	Response of the sensor (m V^{-1})
$\Re(Z)$	Real part of the coil impedance (Ω)
$N_{\mathrm{V}}(\omega)$	Input referred voltage noise (V/$\sqrt{\mathrm{Hz}}$]
$N_{\mathrm{A}}(\omega)$	Input referred current noise (A/$\sqrt{\mathrm{Hz}}$]

A.1. LVDT

Linear variable differential transformers (LVDTs) [25] measure the relative displacement between two stages of the AEI-SAS. The LVDT emitter coil is mounted onto the isolated stage of the AEI-SAS and is driven with a sine wave at 15 kHz using a Texas Instruments DRV134. Two larger counter-wound receiver coils connected together in series are mounted to the ground coaxially and equidistant from the emitter coil. Any relative displacement between the receiver coils and emitter coil will excite a sine wave in the receiver coils which is proportional to the displacement. This signal is amplified using Texas Instruments INA128 differential amplifiers and demodulated using Analog Devices AD630. The relevant noise sources of the LVDTs are the Johnson noise of the excitation and sensing coils

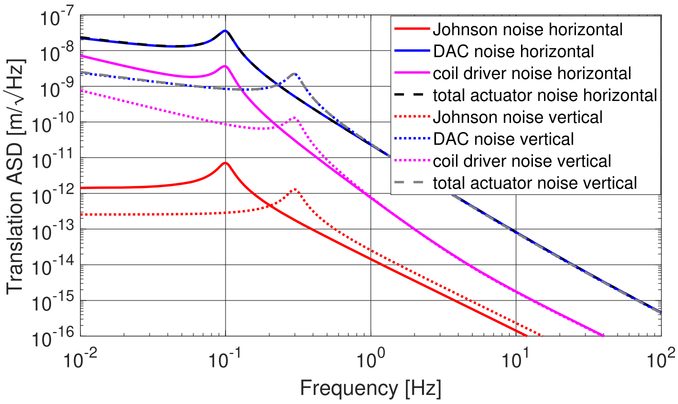

Figure A1. Noise of the voice-coil actuators. The noise of the data acquisition system (see appendix A.5) dominates the total noise over the whole frequency range of interest from 10^{-2} to 10^{2} Hz. The curves labeled with 'Johnson noise' refer to the Johnson noise of the actuator coils.

and the voltage and current noise of the listed differential amplifier, the demodulator and the driver. As relative sensors, the LVDTs also contribute unwanted signal above 0.1 Hz which, although is not noise, is detrimental to the active isolation of the AEI-SAS as discussed in section 4.2.

A.2. Voice-coil actuator

The voice-coil actuators are based on the magnetic interaction of a solenoid and permanent magnets. The design of the voice-coil actuators used in the AEI-SAS is the same as the design in [26].

Figure A1 shows the different noise contributions of the horizontal and vertical voice-coil actuators as equivalent optical table displacement. The noise of the digital-to-analog converter is the dominant noise source. The feed-back loop suppresses the actuator noise below unity gain and above unity gain the actuator noise is sufficiently low. The actuator noise therefore does not limit the active isolation at any frequency.

A.3. Accelerometer

The accelerometers used in the AEI-SAS are custom-built monolithic Watt's linkages. They are based on the design in [27] and measure horizontal inertial motion. A miniature LVDT reads out the position of the reference mass suspended as a fold pendulum. This signal is utilized as an error signal for a feed-back loop which holds the position of the mass with a small voice-coil actuator. This control loop has a bandwidth of approximately 3 Hz. The readout electronics and coil-driver electronics are the same as for the LVDTs.

The accelerometer read out signal is a combination of the feed-back signal that is used to keep the reference mass in place, and the residual error signal. The feed-back signal, which is proportional to force applied to the mass and hence its acceleration, is the dominant accelerometer signal up to 3 Hz. Above 3 Hz, the residual error signal is dominant, which is proportional to inertial displacement of the accelerometer housing.

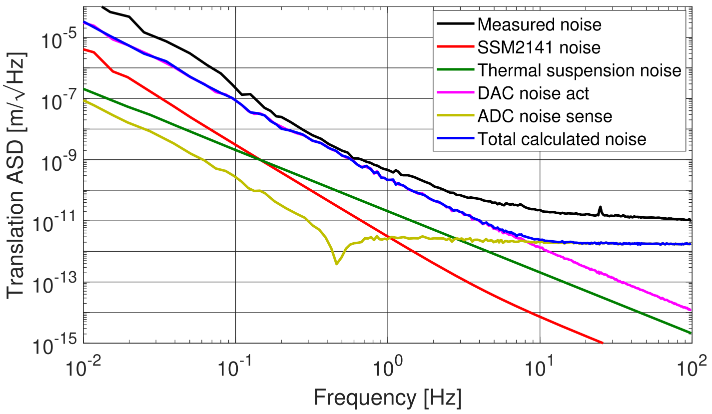

Figure A2. Calculated and measured noise of the monolithic accelerometers. The noise of the data acquisition system contributes to the total noise on two paths. Firstly by influencing the actuation signal that keeps the reference mass in place (‘DAC noise act’). Secondly it contributes by influencing the residual motion signal dominating above 3 Hz (‘ADC noise sense’). The Johnson noise of the readout coils and actuation coil is negligible. The measured noise in black is the result of a huddle test. It matches around 0.4 Hz and deviates below and above this frequency.

Figure A2 shows the noise measurement of an accelerometer using a technique known as a huddle test [28], and is compared against the calculated noise contributions. The noise contributions considered were the voltage noise of the differential amplifier Analog Devices SSM2141, the thermal suspension noise of the Watt’s linkage, and the noise of the data acquisition device (see appendix A.5). The data acquisition noise could be mitigated by pre-amplifying signals prior to digitization at the frequencies limited by noise to increase the dynamic range. The implementation of this for the accelerometers will be unlikely due to the impending upgrade to horizontal geophones. The calculations agree with the measurement only at around 0.4 Hz. The discrepancy is likely a result of the huddle test not being performed under vacuum as the accelerometers are very sensitive to air currents.

A.4. Geophone

Geophones are inertial sensors which measure the motion of a reference mass suspended using a spring. In the AEI-SAS, vertical L-4C geophones are used. A magnet is attached to the reference mass and is positioned within a coil mounted to the housing. Relative motion between the mass and the housing induces a current in the coil. The signal is amplified by a configuration of three operational amplifiers Texas Instruments OPA188, which have low noise at low frequencies.

The response of a geophone is dependent on the relative motion between the mass and its surroundings. This gives a $1/f^2$ slope below the resonance frequency of 1 Hz and a flat slope above. The inductive readout is sensitive to velocity and hence adds another $1/f$ over the whole frequency range when projected into displacement. Overall, the geophone response to displacement has a $1/f^3$ slope below and a $1/f$ slope above the resonance frequency. The relevant noise contributions for the L-4C geophones are the thermal suspension noise of the spring, the Johnson noise of the readout coil and the voltage noise of the OPA188. Figure A3 shows the results of the noise calculation and the huddle test measurements [28].

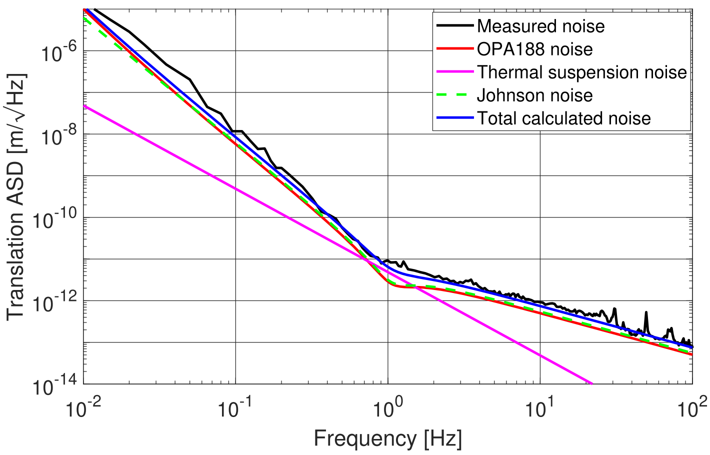

Figure A3. Calculated and measured noise of the L-4C geophones. The OPA188 noise and the Johnson noise of the geophone coil equally dominate the total noise over the whole frequency range of interest. The thermal suspension noise of the spring contributes only around the resonance frequency of 1 Hz.

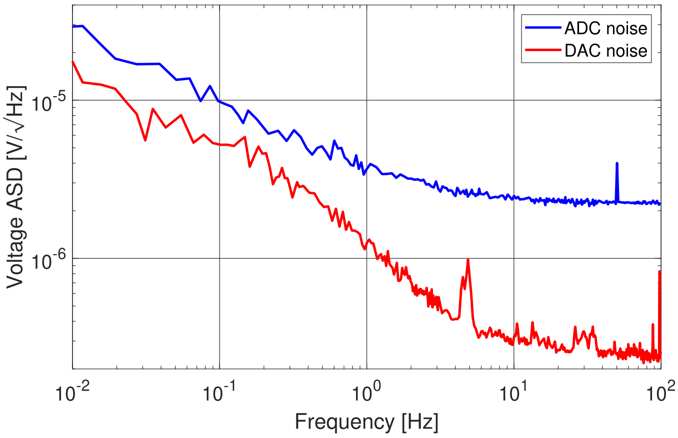

Figure A4. Noise of the ADCs and the DACs of the AEI 10 m prototype. The DAC noise measurement is stitched together from a low and a high frequency measurement.

A.5. Data acquisition device

The sensor signals are digitized by analog-to-digital (ADC) converters. The ADCs have a resolution of 16 bits and a sampling rate of 1 kHz down sampled from 64 kHz. In addition, anti-aliasing filters, consisting of two Sallen–Key low-pass filters with corner frequencies of 10 kHz, are used. The data is processed and analyzed with the ‘Control and Data System’ [33] developed for the LIGO detectors. Output signals are generated by digital-to-analog converters (DACs). The measured ADC and DAC noise is shown in figure A4.

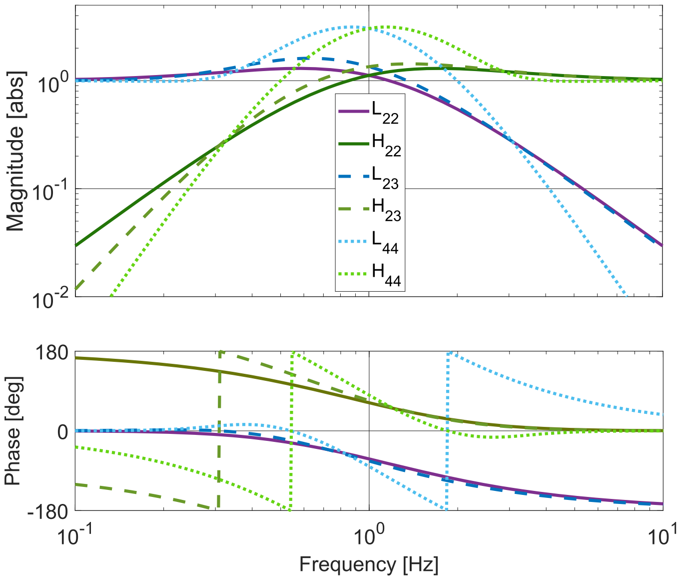

Figure B1. Bode diagram of three combinations of low-pass (L) and high-pass (H) filters. The indices in the filter names refer to the order of the low- and high-pass filter.

Appendix B. Blending Filters

The blending filters used to combine the signals from a pair of sensors consist of a low-pass (L) and a high-pass (H) filter which are complementary, such that their transfer functions satisfy

$$L(s) + H(s) = 1 \tag{B1}$$

where s is the Laplace variable. The blending frequency ω_b is defined as the crossover frequency between the filters where their frequency responses have equal magnitude. We define the filtering order l and h as the frequency dependent order of the attenuation in the stop-bands of the low- and high-pass filters respectively.

The choice of blending filters is influenced by a compromise between stronger attenuation of the noise in the stop-bands and the amplification of noise around the blending frequency due to the filter ripples. Figure B1 shows three different combinations of low- and high-pass filters to exhibit the different slopes and ripples around the blending frequency.

The following will provide an example of the generation of a second-order low- and a second-order high-pass blending filter. Starting with equation (B1), we can substitute the right hand side with a fraction consisting of an equal binomial expression for the numerator and denominator, $(\alpha + s)^{l+h-1}$, where α is a real valued variable. The expressions for the low- and high-pass filters are found by taking the binomial expansion of the numerator and separating

Table B1. Correction factors for blending frequency.

C_{23}	C_{32}	C_{24}	C_{42}	C_{34}	C_{43}
0.6896	$(0.6896)^{-1}$	0.5329	$(0.5329)^{-1}$	0.7773	$(0.7773)^{-1}$

it into the h lowest and l highest s-order terms.

$$\begin{aligned} L_{22}(s)+H_{22}(s) &= \frac{(\alpha+s)^3}{(\alpha+s)^3} = \frac{(\alpha^3+3\alpha^2 s+3\alpha s^2+s^3)}{(s+\alpha)^3} \\ L_{22}(s) &= \frac{(\alpha^3+3\alpha^2 s)}{(s+\alpha)^3} \\ H_{22}(s) &= \frac{(3\alpha s^2+s^3)}{(s+\alpha)^3}. \end{aligned} \tag{B2}$$

The indices of L_{lh}, H_{lh} refer to the low-pass and high-pass filtering order.

The value of α is found by looking at the frequency response at the blending frequency by setting $s = i\omega_{\mathrm{b}}$. The magnitude of the two filters are equal at the blending frequency, by definition, and so

$$|L_{22}(s)|_{s=i\omega_{\mathrm{b}}} = |H_{22}(s)|_{s=i\omega_{\mathrm{b}}} \tag{B3}$$

The squares of the magnitudes of the numerators in equation (B3) can be equated to give

$$(\alpha^3)^2 + (3\alpha^2\omega_{\mathrm{b}})^2 = (-3\alpha\omega_{\mathrm{b}}^2)^2 + (-i\omega_{\mathrm{b}}^3)^2 \tag{B4}$$

Inspection of equation (B4) shows that the non-trivial solution is $\alpha = \pm\omega_{\mathrm{b}}$.

The condition that $\alpha = \pm\omega_{\mathrm{b}}$ is only true for a symmetric pair of blending filters with equal filtering orders, $l = h$. The following example considers a 2nd order low-pass and a 3rd order high-pass filter with:

$$L_{23}(s)+H_{23}(s) = \frac{(\alpha^4+4\alpha^3 s+6\alpha^2 s^2)}{(s+\alpha)^4} + \frac{(4\alpha s^3+s^4)}{(s+\alpha)^4} \tag{B5}$$

Again, by equating the squares of the magnitudes of the numerators for the low- and high-pass filters it is found that the purely real, non-trivial solution is

$$\alpha = \omega_{\mathrm{b}} \cdot C_{23}, \tag{B6}$$

where C_{lh} is a correction factor for the blending frequency, which varies for different filter orders with $l \neq h$. Table B1 shows the correction factor values for blending filter combinations up to an order of 4, which were calculated numerically.

Figure B1 shows the Bode plots of the example blending filters above as well as a pair of fourth-order filters, all with a blending frequency at 1 Hz. This shows that the ripple around the blending frequency increases with the filter order. The peak magnitude of the ripple is 1.30 for L_{22} and H_{22}, 1.43 for L_{23}, 1.61 for H_{23} and 3.14 for L_{44} and H_{44}.

ORCID iDs

R Kirchhoff https://orcid.org/0000-0003-0224-8600

References

[1] Abbott B P *et al* 2016 *Phys. Rev. Lett.* **116** 131103
[2] Robertson D I, Morrison E, Hough J, Killbourn S, Meers B J, Newton G P, Robertson N A, Strain K A and Ward H 1995 *Rev. Sci. Instrum.* **66** 4447
[3] Sannibale V, Abbott B, Aso Y, Boschi V, Coyne D, DeSalvo R and Marka S 2008 *J. Phys.: Condens. Matter.* **122** 012010
[4] Ward R L *et al* 2008 *Class. Quantum Grav.* **25** 114030
[5] Westphal T *et al* 2012 *Appl. Phys. B: Lasers Opt.* **106** 551–7
[6] Acernese F *et al* 2020 *J. Phys.: Condens. Matter.* **1342** 012010
[7] Wanner A 2013 Seismic Attenuation System (AEI-SAS) for the AEI 10m prototype *PhD Thesis* Gottfried Wilhelm Leibniz Universitaet Hannover Technische Informationsbibliothek und Universitaetsbibliothek Hannover (TIB)
[8] Bergmann G *et al* 2017 *Class. Quantum Grav.* **34** 065002
[9] Westphal T 2016 A coating thermal noise interferometer for the AEI 10 m prototype facility *PhD Thesis* Gottfried Wilhelm Leibniz Universitaet Hannover Technische Informationsbibliothek und Universitaetsbibliothek Hannover (TIB)
[10] Pinoli M, Blair D G and Ju L 1993 *Meas. Sci. Technol.* **4** 995–9
[11] Takamori A *et al* 2007 *Nucl. Instrum. Methods Phys. Res.* A **582** 683–92
[12] Cella G, DeSalvo R, Sannibale V, Tariq H, Viboud N and Takamori A 2002 *Nucl. Instrum. Methods Phys. Res.* A **487** 652–60
[13] Takamori A, Ando M, Bertolini A, Cella G, DeSalvo R, Fukushima M, Iida Y, Jacquier F, Kawamura S and Marka S 2002 *Class. Quantum Grav.* **19** 1615
[14] Losurdo G *et al* 1999 *Rev. Sci. Instrum.* **70** 2507–15
[15] Losurdo G *et al* 2001 *Rev. Sci. Instrum.* **72** 3653–61
[16] Braccini S *et al* 2005 *Astropart. Phys.* **23** 557–65
[17] Akutsu T *et al* 2017 arXiv:1710.04823 [gr-qc]
[18] Wen S *et al* 2014 *Class. Quantum Grav.* **31** 235001
[19] Matichard F *et al* 2015 *Class. Quantum Grav.* **32** 185003
[20] Beker M G 2013 Low-frequency sensitivity of next generationgravitational wave detectors *PhD Thesis* Free University Amsterdam
[21] Beker M G, Bloma M, van den Brand J F J, Bulten H J, Hennes E and Rabeling D S 2012 *Phys. Procedia* **37** 1389–97
[22] Bertolini A *et al* 2006 *Class. Quantum Grav.* **23** S111
[23] Stochino A *et al* 2009 *Nucl. Instrum. Methods Phys. Res.* A **598** 737–53
[24] Accadia T *et al* 2010 *Class. Quantum Grav.* **27** 194011
[25] Tariq H *et al* 2002 *Nucl. Instrum. Methods Phys. Res.* A **489** 570–6
[26] Wang C, Tariq H, DeSalvo R, Iida Y, Marka S, Nishi Y, Sannibale V and Takamori A 2002 *Nucl. Instrum. Methods Phys. Res.* A **489** 563–9
[27] Bertolini A, DeSalvo R, Fidecaro F, Francesconi M, Marka S, Sannibale V, Simonetti D, Takamori A and Tariq H 2005 *Nucl. Instrum. Methods Phys. Res.* A **556** 616–23
[28] Kirchhoff R *et al* 2017 *Rev. Sci. Instrum.* **88** 115008
[29] Matichard F and Evans M 2015 *Bull. Seismol. Soc. Am.* **105** 497–510
[30] Koehlenbeck S 2018 Towards the SQL interferometer length stabilization at the AEI 10 m-prototype *PhD Thesis* Gottfried Wilhelm Leibniz Universitaet Hannover Technische Informationsbibliothek und Universitaetsbibliothek Hannover (TIB)
[31] Wipf C 2014 Noise Budgeting for Advanced Detectors (https://dcc.ligo.org/LIGO-G1400587/public)
[32] Barzilai A, VanZandt T and Kenny T 1998 *Rev. Sci. Instrum.* **69** 2767–72
[33] Bork R, Abbott R, Barker D and Heefner J 2001 arXiv:physics/0111077 [physics.ins-det]